JGR Planets

RESEARCH ARTICLE
10.1029/2022JE007277

Special Section:
ExoMars Trace Gas Orbiter - One Martian Year of Science

This article is a companion to Trompet et al. (2023), https://doi.org/10.1029/2022JE007279.

Key Points:

- We show global vertical distributions of CO_2 and temperature with high resolution in the Mars mesosphere at the terminator
- Many mesospheric temperature profiles at the terminator present an inversion layer with a warm layer around 0.1 Pa
- The distribution of warm layers is similar in Martian years 35 and 36. Warm layers are absent at dusk in the South hemisphere at L_s 50°–150°

Supporting Information:

Supporting Information may be found in the online version of this article.

Correspondence to:

L. Trompet,
loic.trompet@aeronomie.be

Citation:

Trompet, L., Vandaele, A. C., Thomas, I., Aoki, S., Daerden, F., Erwin, J., et al. (2023). Carbon dioxide retrievals from NOMAD-SO on ESA's ExoMars Trace Gas Orbiter and temperature profiles retrievals with the hydrostatic equilibrium equation: 1. Description of the method. *Journal of Geophysical Research: Planets*, *128*, e2022JE007277. https://doi.org/10.1029/2022JE007277

Received 2 MAR 2022
Accepted 7 SEP 2022

Carbon Dioxide Retrievals From NOMAD-SO on ESA's ExoMars Trace Gas Orbiter and Temperature Profiles Retrievals With the Hydrostatic Equilibrium Equation: 1. Description of the Method

L. Trompet[1], A. C. Vandaele[1], I. Thomas[1], S. Aoki[1,2], F. Daerden[1], J. Erwin[1], Z. Flimon[1], A. Mahieux[1,3], L. Neary[1], S. Robert[1,4], G. Villanueva[5], G. Liuzzi[5,6], M. A. López-Valverde[7], A. Brines[7], G. Bellucci[8], J. J. López-Moreno[7], and M. R. Patel[9]

[1]Royal Belgian Institute for Space Aeronomy, Brussels, Belgium, [2]Department of Complexity Science and Engineering, Graduate School of Frontier Sciences, The University of Tokyo, Kashiwa, Japan, [3]The University of Texas at Austin, Austin, TX, USA, [4]Institute of Condensed Matter and Nanosciences, Université catholique de Louvain, Louvain-la-Neuve, Belgium, [5]Goddard Flight Space Center (GFSC), Greenbelt, MD, USA, [6]Department of Physics, American University, Washington, DC, USA, [7]Instituto de Astrofisica de Andalucia (IAA/CSIC), Gta. de la Astronomía, Granada, Spain, [8]Istituto di Astrofisica e Planetologia Spaziali (IAPS/INAF), Rome, Italy, [9]School of Physical Sciences, The Open University, Milton Keynes, UK

Abstract The Solar Occultation (SO) channel of the Nadir and Occultation for Mars Discovery (NOMAD) instrument has been scanning the Martian atmosphere for almost 2 Martian years. In this work, we present a subset of the NOMAD SO data measured at the mesosphere at the terminator. From the data set, we investigated 968 vertical profiles of carbon dioxide density and temperature covering the Martian Year (MY) 35 as well as MY 36 up to a solar longitude (L_s) of 135° and altitudes around 60–100 km. While carbon dioxide density profiles are directly retrieved from the spectral signature in the spectra, temperature profiles are more challenging to retrieve as unlike density profiles, temperature profiles can present some spurious features if the regularization is not correctly managed. Comparing seven regularization methods, we found that the expected error estimation method provides the best regularization parameters. The vertical resolution of the profiles is on average 1.6 km. Numerous warm layers and cold pockets appear in this data set. The warm layers are found in the Northern hemisphere at dawn and dusk as well as in the Southern hemisphere at dawn. Strong warm layers are present in more than 13.5% of the profiles. The Southern hemisphere at dusk does not present any warm layer between L_s 50° and 150°. The height and latitudinal distribution of those warm layers were similar in MY 35 and MY 36 during the first half of the year (L_s = 0°–135°).

Plain Language Summary Martian mesosphere (the region of the atmosphere between 50 and 100 km in altitude) is the place where many large and small-scale thermal features occur, which necessitates observations made at a fine spatial resolution. The Solar Occultation (SO) channel of the Nadir and Occultation for Mars Discovery (NOMAD) instrument is an infrared spectrometer sensitive in a spectral range where CO_2, H_2O, CO, and CH_4 have spectral signatures. NOMAD-SO probes the Martian atmosphere with a high signal-to-noise ratio and a fine vertical sampling using the solar occultation technique. We implemented a scheme to fine-tune the regularization of the vertical profiles leading to the best possible resolution of the retrieved profiles. We show here almost a year and a half of the measurements of carbon dioxide density and temperature of the Mars mesosphere at the terminator, that is, the separation between the day side and the night side. On average, the mesosphere is characterized by a decrease in the temperature with height. At the high resolution achieved here, we highlight many warmer layers in the Northern hemisphere and also in the Southern hemisphere at dawn but not at dusk. Stronger warm layers are found around the perihelion.

1. Introduction

The mesosphere of Mars is the region of the atmosphere from around 50–100 km and is currently one of the main regions of interest where several important atmospheric phenomena occur such as gravity waves (Nakagawa, Terada, et al., 2020; Saunders et al., 2021; Starichenko et al., 2021) and/or tides (England et al., 2019; Gröller et al., 2018; Jain et al., 2021; Nakagawa, Jain, et al., 2020). The mesosphere is the coldest region in the atmosphere of Mars and the temperature can be so low that CO_2 freezes into ice clouds (Liuzzi et al., 2021). Also,

recently, an intense warm layer was detected on the night side of Mars (Nakagawa, Jain, et al., 2020). There is a need for high-resolution temperature profiles as all those atmospheric phenomena are related to the thermal structure of the mesosphere.

Most of the recently published Mars mesospheric temperature profiles are derived from three instruments. The Mars Climate Sounder (McCleese et al., 2007) onboard Mars Reconnaissance Orbiter regularly sounds the temperature of the troposphere and the mesosphere around local times of 3 and 15 hr and with a vertical resolution of 5 km (Shirley et al., 2015). MAVEN-IUVS uses the stellar occultation technique which allows probing at any local time but still more often in the nightside, with a vertical resolution from 2 to 10 km (Gröller et al., 2015; Nakagawa, Jain, et al., 2020). More recently, Alday, Trokhimovskiy et al. (2021), Alday, Wilson et al. (2021), and Fedorova et al. (2020) reported some temperature profiles at the terminator from the ACS instrument on board TGO for the second half of the MY 34 and also MY 35 in Alday, Trokhimovskiy et al. (2021). Belyaev et al. (2021) also reported ACS temperature profiles for the second half of the both MY 34 and 35. The vertical resolution of those profiles is between 1 and 3 km.

Also on board TGO, the Nadir and Occultation for Mars Discovery-Solar Occultation (NOMAD-SO) (SO in the following) channel (Vandaele et al., 2015) scans the Martian atmosphere using solar occultation since 21 April 2018. One of its objectives is to provide high-resolution CO_2 density and temperature vertical profiles with ranges extending from a few kilometers above the surface up to around 200 km. The high vertical resolution of those profiles is sufficient to resolve small features such as inversion layers or gravity waves.

The aim of these SO profiles is to improve our understanding of Mars climatology at the terminator from the troposphere to the thermosphere. But temperature profiles are also important for the density retrieval of species such as water and carbon monoxide as their spectral signature depends on temperature. Profiles of carbon dioxide are also valuable information to derive the volume mixing ratio of other species as it constitutes around 95% of the Martian atmosphere in the homosphere (Franz et al., 2017; Owen et al., 1977).

In this paper, we focus on one particular spectral range from NOMAD-SO, which extends from 3,325 to 3,352 cm^{-1} and is dedicated to inferring carbon dioxide and temperature profiles of the mesosphere.

As SO performs SO, all derived profiles are located at the terminator of the atmosphere, that is, the transition region between the day and night sides already probed by MAVEN-IUVS and MRO-MCS.

The retrieval method relies on a retrieval algorithm developed by Quémerais et al. (2006) and is widely used to retrieve density and temperature (Forget et al., 2009; Gröller et al., 2018; Koskinen et al., 2013; Sandel et al., 2015). We further improved this method by fine-tuning the regularization. The temperature profiles are derived from the CO_2 density profiles with the hydrostatic equilibrium equation. We derived 968 temperature profiles spread from MY 35 to MY 36 with a solar longitude (L_s) of 135° (23 March 2018–31 November 2021).

In this first part of a series of two papers dedicated to the observation of CO_2 and temperature from NOMAD-SO observations, we focused on the description of the method and in particular the vertical inversion from slant quantities to vertical local quantities. In the second part of this series (Trompet et al. (2023), hereafter called Part II), we will investigate in more detail the results concerning CO_2 and temperature, looking at latitudinal and time variations, as well as comparing them with other instruments' results and GCM. In addition, a companion paper by López-Valverde et al. (2022) this issue presents another analysis of temperatures and densities, although focused on MY34.

2. Materials and Methods

2.1. The NOMAD-SO Channel

The NOMAD instrument on board ESA's Trace Gas Orbiter is a suite of three spectrometers (Neefs et al., 2015): Uv and VISible (UVIS), Limb, Nadir, and Occultation (LNO), and SO. The operating spectral ranges of the UVIS, LNO, and SO channels are 200–650 nm, 2.2–3.8, and 2.2–4.2 μm, respectively. While UVIS and LNO can operate in a limb, nadir and solar occultation observing modes, SO is dedicated only to solar occultation. This observing mode consists of keeping the instrument line of sight (LoS) pointing to the Sun and sweeping the planet's atmosphere along the orbit of the spacecraft.

SO is composed of an echelle grating and an Acoustic-Optical Tunable Filter (AOTF) for the diffraction order selection. The echelle grating has a high Blaze angle (67.73°) to diffract most of the light intensity in higher diffraction orders extending from 110 to 200. The grating's free spectral range (FSR), characterizing also the width

of the blaze function, is around 22.56 cm^{-1} and varies with the temperature inside the instrument (Villanueva et al., 2022). The spectral range extending on the detector is 19.6 for order 110 (2,471.7–2,491.3 cm^{-1}) and 35.7 cm^{-1} for order 200 (4,494.0–4,529.7 cm^{-1}) and the resolving power ($\lambda/d\lambda$) is 17,000. The AOTF exploits Bragg diffraction for light filtering and is composed of a transducer that induces acoustic waves in a TeO_2 crystal. The acoustic waves periodically modify the refractive index of the crystal and the AOTF tunes the light filtering by changing the frequency of the acoustic waves. The AOTF transfer function is the Fourier transform of the plane parallel wave entering the crystal and thus follows a sine cardinal square (sin c^2) function. The AOTF mainly selects one diffraction order as the widths of the AOTF transfer function and the blaze function are similar. Signals from adjacent orders are also present on the observed spectra due to the side lobes of the AOTF transfer function, which are characterized using dedicated solar calibration measurements (Villanueva et al., 2022).

During an occultation, SO records five or six diffraction orders every second. In the latter case, the dark current is subtracted on-board, while in the former case, the dark current is recorded as a sixth diffraction order and downlinked.

The detector is composed of 320 pixels along the spectral axis and 256 rows in the spatial direction, but only 16 lines over 256 are enough illuminated and selected. The spatial direction is tilted by 23° with respect to the horizon. Due to downlink limitation, those 16 lines are binned into four spectra of four lines that we call hereafter "bins." In nominal operations, SO scans thus four spectra of 320 pixels times six diffraction orders per second (Thomas et al., 2021). The illumination is almost constant along the 16 lines and the variability within one bin is smaller than 2% (see Figure 8 in Thomas et al., 2021). The projection of one bin on the tangent point, that is, the field of view (FOV) of one bin, varies between 1.70 and 1.86 km for altitudes between 50 and 100 km and considering the slit tilted by 23°. The vertical sampling is on average 250 m with a standard deviation of 175 m as the vertical sampling varies from one orbit to another mainly with the beta-angle, that is, the angle of the TGO's orbit to the Mars-Sun vector. The spatial resolution is mainly restricted by the FOV and varies between 2 and 5 km with an average of 2.5 km. The SNR of the measurements is on average 2,500 around pixel 180 and decreases on the sides of the spectrum.

2.2. Spectral Range

The NOMAD-SO spectral range covers 2,400–4,600 cm^{-1} and sweeps many CO_2 spectral bands. The spectral line intensities of the CO_2 bands are represented in Figure 1. Water is present in almost all the NOMAD-SO spectral range. The intensities of some water lines are higher than the CO_2 ones, but the water lines appear weaker on NOMAD-SO spectra water is much less abundant. The main CO_2 fundamental bands are the $\nu_1 + \nu_3$ band in orders 163–166, the $2\nu_1 + \nu_2$ band in order 147–149 and the $\nu_2 + \nu_3$ band in order 132 which are suitable to probe, respectively, the mid and upper thermosphere, the mesosphere and the troposphere. The other bands will be reported in further studies. The two first bands are due to the main isotopologue ($^{12}C^{16}O_2$), while the last one is for the isotopologue $^{16}O^{12}C^{18}O$.

The main diffraction order used in this work is 148 covering from 3,325.6 to 3,351.9 cm^{-1} when the instrument has a temperature of 0°C (see Section 2.4 for the wavenumber calibration with temperature). The instrument temperature varies between −15°C and 5°C, which induces a maximum variation of 1.4 cm^{-1}. The number of CO_2 lines always remains the same for all those spectral variations. We consider signals from plus and minus four adjacent diffraction orders (so nine orders in total) in the radiative transfer calculations, corresponding to 3,280.6 to 3,397.2 cm^{-1}. Figure 3 shows some spectra of order 148. The strong CO_2 features appearing in this diffraction order are the fundamental band $2\nu_1 + \nu_2$, or 21102-00001 in AFGL (U.S. Air Force Geophysics Laboratory) code (Rothman & Young, 1981) containing a Q branch in the middle of order 148. Water lines are also present in the spectral range around order 148, but they are negligible at the altitudes considered in this work (higher than 60 km).

2.3. Data Coverage

From the beginning of the mission until 1 December 2021, there are 3,229 scans of diffraction orders either 147 (3,303.1–3,329.3 cm^{-1}), 148, or 149 (3,348.0–3,374.6 cm^{-1}) which contain a suitable spectral range to retrieve CO_2 density vertical profiles in the mesosphere. In this study, we have decided to focus on order 148 only, from the beginning of MY 35 for $L_s = 0°$–135° in MY 36. As represented in Figures 2a and 2c, the 968 profiles (656 in MY 35 and 312 in MY 36) cover most of the latitudes even though the equator region (−30° to 30°) is less well covered than the highest latitudes. The covered local time (Figures 2b and 2d) changes with the latitudes. The solar local time is restricted to 6 or 18 hr at the equator.

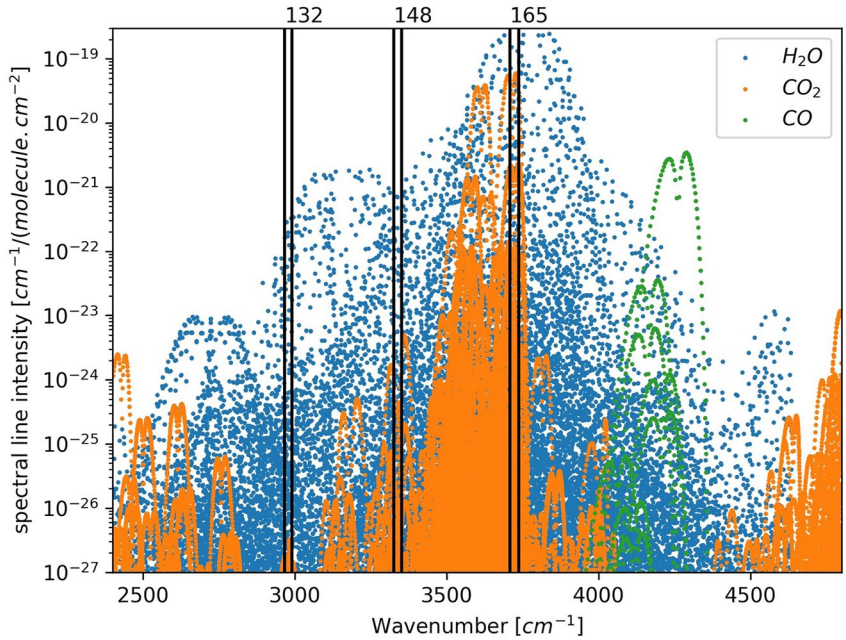

Figure 1. Spectral line intensities in the Nadir and Occultation for Mars Discovery-Solar Occultation spectral range for CO_2 in orange, H_2O in blue and CO in green. The extension of the main diffraction orders are represented with black vertical lines.

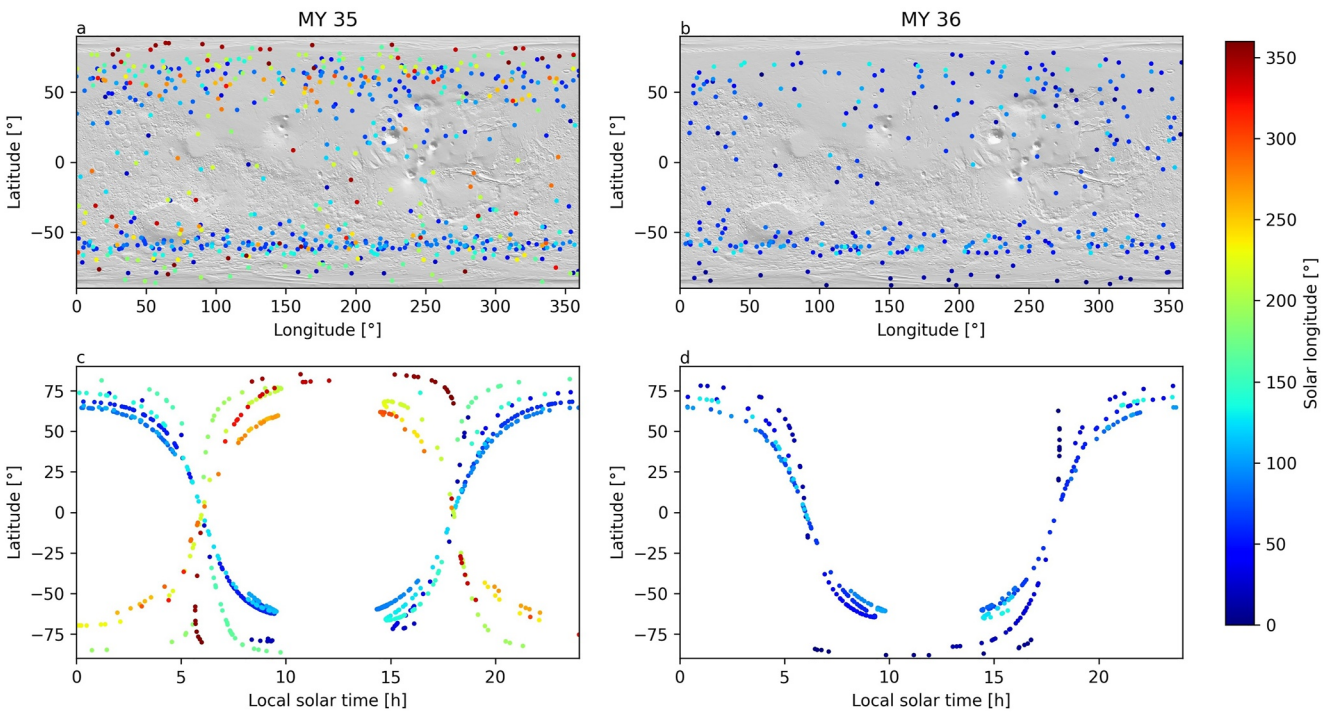

Figure 2. Coverage of the 655 selected profiles in Martian Year (MY) 35 for latitude as a function of longitude in panels (a) and latitude as a function of solar local time in panel (c). Same for the 308 profiles in MY 36 in panels (b and d). From panels (a and b), most of the latitudes scanned are close to ±60°. Panels (c and d) present typical local solar time coverage for solar occultation: scans at the equator are close to 6 and 18 hr and deviate toward the poles. Local solar times closer to 12 hr are reached in the hemisphere, which is closer to the summer solstice.

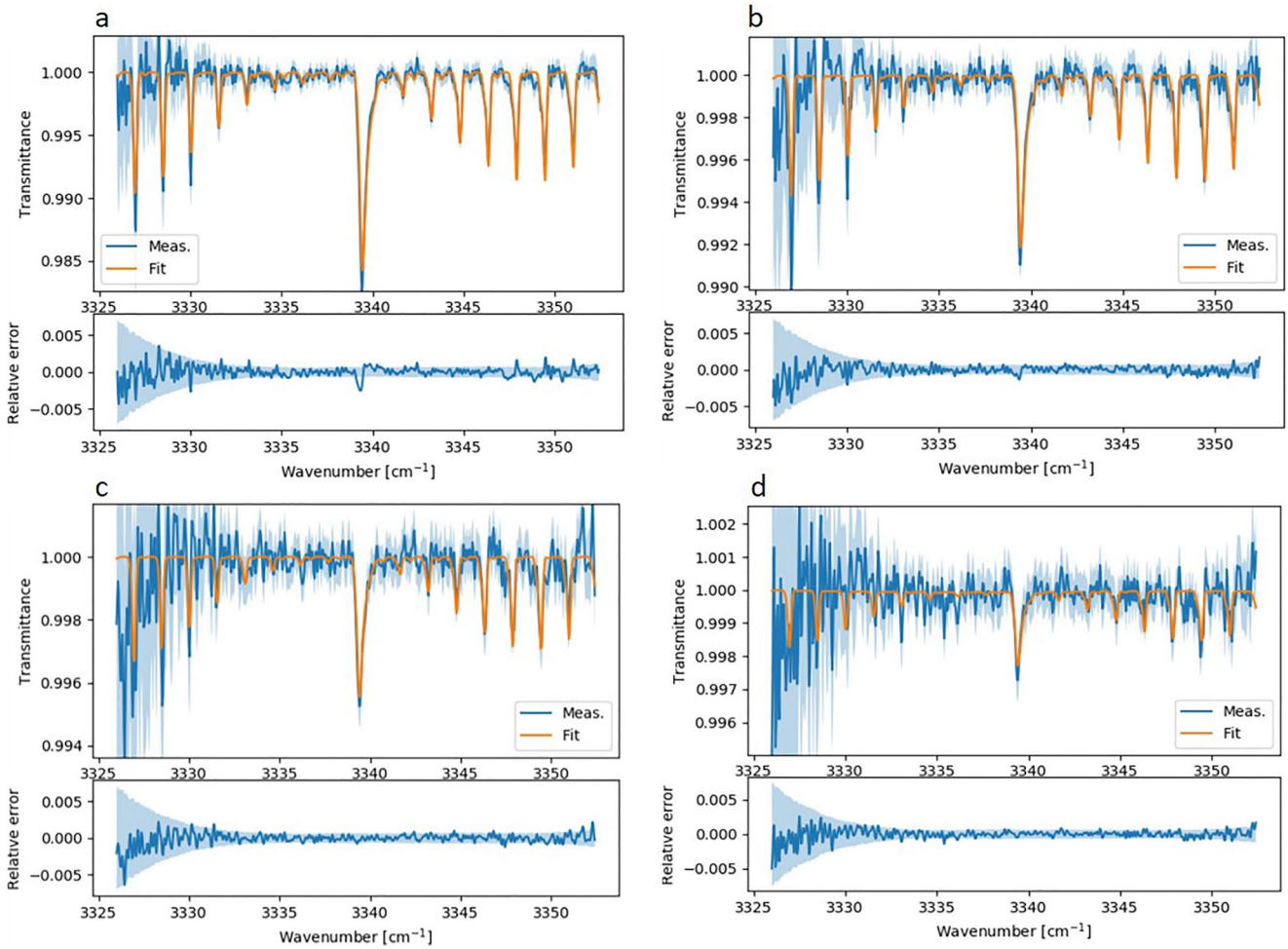

Figure 3. Nadir and Occultation for Mars Discovery-Solar Occultation transmittance spectra in blue and fitted spectra in orange in the upper panels for 20190526_141013_1p0a_SO_A_I_148 at altitudes (a) 70, (b) 75, (c) 80, and (d) 85 km. The lower panels represent the relative difference: (Meas.-Fit)/Meas. The shaded area is the uncertainty in the transmittance spectrum (Meas.). Higher uncertainties on the left-hand side of the spectra are due to a lower strength of the signal at those pixels.

2.4. Calibration

A preliminary calibration of the NOMAD SO IR channel was derived by Liuzzi et al. (2019). It contains the models for the AOTF function, the grating's Blaze function and the instrument line shape (ILS). The calibration of all those functions has been extensively updated since then (e.g., Villanueva et al., 2022). The AOTF function is modeled with an asymmetrical sin c^2 function plus a broad Gaussian background. The FSR of the Blaze function changes with the temperature of the instrument and the ILS is modeled with a double Gaussian (Thomas et al., 2021). These refined instrumental functions/coefficients are used in this study. In addition, some other modifications are applied as summarized in the Section S2 in Supporting Information S1. In the following, we use Level 1.0 data, which correspond to transmittances. Those transmittance spectra were obtained by applying a method based on Trompet et al. (2016) but updated for NOMAD (see Section S1 in Supporting Information S1).

3. Retrieval Method

The retrieval method is split into three main steps:

- Step-1: the total column densities of CO_2 along the LoS (hereafter "slant column") are retrieved for each spectrum with the ASIMUT program.

- Step-2: the retrieved vertical profiles of slant column number densities are inverted into vertical profiles of local number densities with a method similar to Quémerais et al. (2006),
- Step-3: the temperature profiles are computed from the hydrostatic equilibrium equation.

The algorithm then goes back to Step 1 using the updated temperature profile. Several loops are needed to reach convergence and give more strength to the retrieved values. The main advantage of separating the vertical inversion from the spectral inversion is to rapidly fine-tune the regularization of the density profile. This is particularly important as the retrieved temperature profile is sensitive to any variations in the CO_2 density profile.

3.1. Spectral Inversion (Step-1)

In Step 1 of the procedure, the ASIMUT radiative transfer program (Vandaele et al., 2006) was employed (see Section S3 in Supporting Information S1 for the details of the retrieval).

The spectral inversion is the most computationally expensive step. This is mainly due to the computation of the absorption coefficients with a fine spectral grid and convolution of them with the instrumental functions. Nevertheless, this inversion is easily parallelized as the retrieval of each spectrum is independent. The Gauss-Newton iteration usually converges after four iterations.

The upper bound of the valid altitude range of a vertical profile corresponds to a spectrum containing enough strong lines to be well fitted. Our criterion for the highest altitude is defined by the degree of freedom (DOF) for the signal, as defined in Rodgers (2000). A DOF equal to unity means that the retrieved value is derived essentially from the information contained in the measurement, while a DOF is close to zero means that the retrieved value is essentially the a priori value. In this work, we only keep retrieved values corresponding to a DOF greater than 0.99, corresponding to averaged relative uncertainty of 15%. This limit corresponds to a slant column of 1.73×10^{20} cm^{-2} and corresponds to an altitude between 80 and 100 km following the CO_2 cycle.

The lower bound is due to the saturation of the CO_2 lines (see Section S4 in Supporting Information S1 for a detailed explanation of the saturation of the CO_2 lines), which occurs when the incident light is already too attenuated to be further absorbed by the following CO_2 molecules on the LoS. When saturation occurs, there is a change in the slope of the curve of the equivalent width to altitude. We define the limit of the profile when the second derivative of the equivalent width to the altitudes equals zero between 45 and 70 km for the Q branch (those altitude values are specific for diffraction order 148). This limit corresponds to a slant column of 1.19×10^{22} cm^{-2} and an altitude between 45 and 70 km. Thick dust layers or clouds can reduce the signal and we do not take into account spectra with a baseline in transmittance lower than 0.3. In practice, this saturation of the lines in diffraction order 148 happens at a higher altitude than the reduction of the baseline due to dust/aerosols and saturation is thus the main constraint on the lowest bound of the profiles.

Typically, the effect of the saturation is to underestimate the retrieved density with respect to the true density. The information contained in the spectra is not lost, but any small change in the fitted line depth will result in an important change in the retrieved density. In addition, the spectra contain errors inherent to measurements and the instrument function is not perfectly known.

This bias can explain the decrease in the retrieved density at 70 km shown in Forget et al. (2009), which was not supported by the GCM calculation as those cross-sections saturate below 90 km, as shown in Figure 7 in Quémerais et al. (2006). A way to extend the lower bound of the profile is to decrease the variance on the a priori, meaning that we assign a strong constraint on the retrieved value to prevent the retrieved value from deviating from the a priori. In this work, we prefer to cut the profile and provide only values that are almost entirely originated from information contained in SO spectra.

Figure 3 shows an example of fitted spectra with ASIMUT for an ingress occultation scanned on 26 May 2019 for order 148. The left-hand side of the spectra is more difficult to constrain as the noise is more important. The residual on the main part of the spectra is lower than 0.0015%.

3.2. Vertical Inversion (Step-2)

The vertical inversion converts a slant column profile c into a vertical profile of local density n. The slant column is the sum of the density along the LoS, and we have $c = Kn$ where K is the Abel transform operator. This assumes that the atmosphere is split into homogeneous layers.

We approximated that the averaged density within two consecutive layers is located in the middle of those two layers (Gröller et al. (2018) and Quémerais et al. (2006)). This induces a bias in the retrieved local density profile. We verified that this bias is negligible if the thickness of the layers is lower than 1 km. The NOMAD-SO vertical sampling being lower than 1 km, this bias is indeed negligible.

We selected only the retrieved slant columns with a DOF higher than 0.99 otherwise high spurious variations appear in the derived temperature profile. This criterion corresponds to a relative uncertainty of around 15% on the slant column. In addition, we also impose the criterion that at least one CO_2 spectral line must have a depth higher than the noise level.

The retrieval method is based on the one developed by Quémerais et al. (2006) and further detailed by Gröller et al. (2018). This method is widely used by the community (see for instance Forget et al., 2009; Gröller et al., 2018; Koskinen et al., 2013; Sandel et al., 2015; Snowden et al., 2013). The inversion method is an iterated Tikhonov (IT) algorithm where the solution is improved using the uncertainties derived from the previous loop. The advantage of an IT algorithm is to improve the accuracy of the regularization of the solution. This algorithm is explained in detail in the Section S5 in Supporting Information S1.

3.2.1. Computation of the Best Regularization Parameter

Tikhonov regularization was first used in Phillips (1962), then detailed in Tikhonov (1963) for the mathematical background, and in Twomey (1963) for atmospheric parameter retrievals. This method relies on a regularization parameter λ_0 which tunes the smoothing of the solution. Many methods were proposed to infer the best λ_0 and we compared seven of those methods with synthetic profiles: the expected error estimation (EEE) described in Xu et al. (2016), but previously used in Steck (2002), Morozov's discrepancy principle (DP—Morozov, 1966), the L-curve method (LC—Hansen, 1992), the generalized cross-validation method (GCV—Golub et al., 1979), the quasi-optimality criterion (QOC—Doicu et al., 2010), the maximum likelihood estimation (MLE—Doicu et al., 2010), and the unbiased predictive risk estimator (UPRE—Doicu et al., 2010).

All those methods require computing many inversions with different λ_0. Thus, splitting the retrieval into a spectral inversion and a vertical inversion is a clear advantage as the vertical inversion is much faster than the spectral inversion with consequential radiative transfer computations.

We tested those seven methods with a known density profile, called n_{true} taken from a profile from GEM-Mars general circulation model (Daerden et al., 2019, 2022; Neary & Daerden, 2018; Neary et al., 2020). We arbitrarily choose an averaged profile for all seasons and locations, but any profile could be used. The point is to reduce the spurious oscillations, which are much smaller than the vertical resolution of the profiles. We converted this density profile into a slant column profile and then added some random noise. We chose seven noise levels extending from 0.1%, 0.5%, 1%, 5%, 10%, 50%, and 100% and computed a thousand samples for each noise level. For each sample, the IT algorithm is tested with a hundred values of λ_0 from 0.001 to 7. We then computed the result for the seven methods which provided their best λ_0 and the corresponding density profile. Finally, we computed the averaged relative error to n_{true} and Figure 4 summarizes the results.

As the noise level of the slant columns increases, the inverted density profiles have higher noise levels because regularization can reduce the noise level but not discard it completely.

The two best methods are the discrepancy principle and the expected error estimation. Those two methods reduce the noise level by an order of magnitude with respect to the quasi-optimal criterion and the maximum likelihood estimation methods.

The expected error estimation searches for a λ_0 that minimizes the total error on the retrieved profile. The total error is the sum of the regularization error, the retrieval noise error, the forward model error, and the instrument model error. In practice, the forward model error and the instrument model error are weakly dependent on λ_0 and are neglected (Xu et al., 2016). The regularization error is a function of the true solution profile that we do not know in practice and we approximate it as in Xu et al. (2016). The expected error estimation method seeks the minimum value of the square of the L2-norm (summation in quadrature) over the total error

$$\|e_{\text{tot}}\|^2 = \|(A - I)n\|^2 + \sigma^2 \text{trace}\left(GG^T\right)$$

where $G = \left(K^T S_c^{-1} K + \lambda_0 L^T S_n^{-1} L\right)^{-1} K^T S_c^{-1}$ is the gain matrix, $A = GK$ is the averaging kernels matrix, I is the identity matrix, σ is the noise on the slant column, S_c is the covariance matrix over the slant columns, S_n is

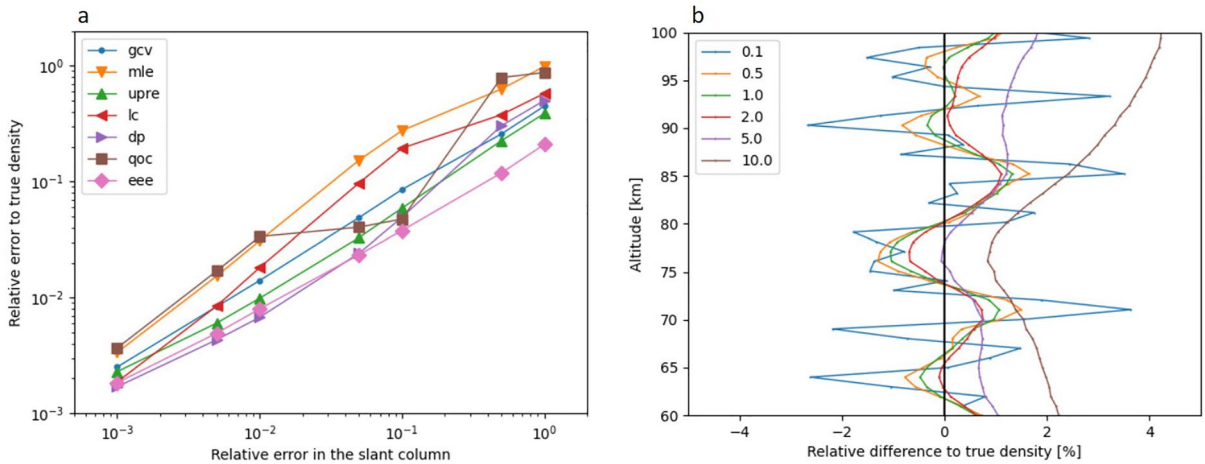

Figure 4. Panel (a): Results from the synthetic test on the seven regularization methods: generalized cross-validation, maximum likelihood estimation, unbiased predictive risk estimator, L-curve, discrepancy principle, quasi-optimality criterion (QOC), and expected error estimation (EEE). The x-axis represents the relative error in the initial slant column and the y-axis represents the averaged final relative error of the retrieved density. We see that the overall best regularization method is the EEE. The QOC method has a less monotonic curve as it passes from undersmoothing at low error to oversmoothing at high error. Panel (b): Example of relative difference to the true density profile ($(n_{\text{true}} - n_{\text{ret}})/n_{\text{true}}$) for different values of λ_0 and for a relative error on the slant column of 1%. From the EEE method, the best value is close to one. As we see, lower values contain spurious peaks and higher values are too smooth and the entire profile diverges from the true density profile. For $\lambda_0 = 2$, the mean value of the profiles starts to deviate from the mean value of n_{true} above 90 km. The profiles deviate further for $\lambda_0 = 5$ and $\lambda_0 = 10$.

the covariance matrix over the density, and L is the second-order differential operator constructed by taking into account the non-regular vertical sampling (Fornberg, 1988). The regularization error is an increasing function of λ_0 while the retrieval noise error is a decreasing function of λ_0 and the sum of these two functions contains a minimum.

The discrepancy principle seeks the regularization parameter for which the residual $\rho = \|Kn - c\|$ equals the noise on the slant column. Morozov's discrepancy principle works slightly better than the expected error estimation for lower noise levels as, in this synthetic test, we know exactly what is the level of noise on which this method strongly depends. For a real case, we approximate the level of error with the uncertainties on the data which are slightly overestimated and the discrepancy principle will provide a higher value for λ_0. Taking those facts into account and considering also that the EEE method performs well for all levels of noise, we decided to keep the EEE method to derive the best λ_0. Rarely, the EEE method does not exhibit a minimum when one of the two terms is an order of magnitude higher than the other one. In this case, we use the discrepancy principle to find the best λ_0.

For the inversion of real NOMAD-SO data, we compute 100 inversions with a λ_0 varying on a log grid from 0.001 to 7 and the solution is then refined using a simplex algorithm (Nelder & Mead, 1965; Virtanen et al., 2020) The computation of λ_0 is at least 10 times faster than the spectral inversion and both are parallelized.

Figure 5 illustrates the method and its results, showing the derived density and temperature profiles for five regularization parameters. The EEE method gives a value of 0.15 as the best regularization parameter. This value represents a compromise between reducing the spurious peaks and not altering the true variability of the profile. Lower values do not have enough smoothed temperature profiles as they still contain spurious oscillations. The oscillations are very small-scale features lower than the vertical resolution of the profiles. For instance, they cannot be misinterpreted with the warm layers discussed in Part II, which are much more spread vertically than the vertical resolution of the profiles. On the other side, the variability of the profile disappears for higher regularization parameters. Over-smoothing removes the true variability and pushes the mean value of the retrieved profile toward the a priori (which is the null vector in this case).

The regularization parameter λ_0 has a log-normal distribution. For all the NOMAD-SO profiles considered in this work, the EEE method provides λ_0 parameters with a geometric mean of 0.18 with a geometric standard deviation factor of 4.7 meaning that λ_0 ranges from 0.039 to 0.84 on a logarithmic scale. This variation is due to the vertical sampling which is a function of the beta-angle of the orbit and the error which is mainly a function of

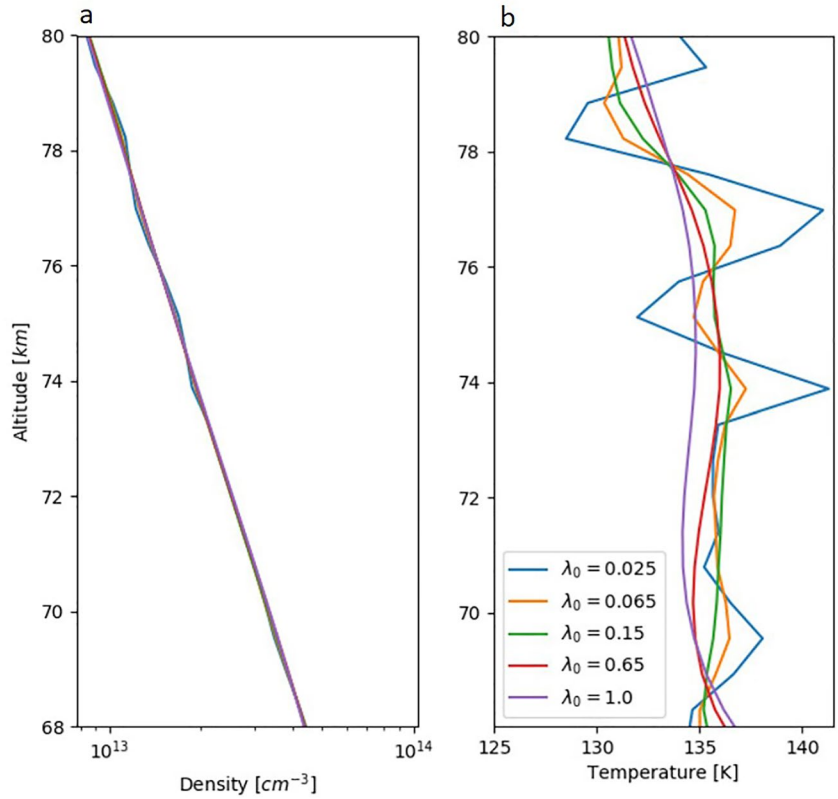

Figure 5. Example of profiles retrieved for occultation 20190504_0202323_1p0a_SO_A_E_148 and for five different regularization parameters. Panel (a) shows the density profiles and panel (b) shows the temperature profiles. The spurious oscillations appear more clearly in the temperature profiles than in the density profiles which are plotted on a logarithmic scale. The best regularization parameter in this particular case is 0.15 (green curve) for the expected error estimation method. The profile for 0.65 starts to deviate below 74 km.

the instrument temperature. Previous studies deriving profiles with the IT algorithm used a single regularization parameter. As the regularization is computed for each profile in this work, we do not need to use another low-pass filtering technique such as the Savitsky-Golay filter as in Gröller et al. (2018) and Snowden et al. (2013).

3.2.2. Vertical Resolution

The vertical resolution depends on the vertical sampling, which depends on the beta-angle, and the regularization, which mainly depends on the level of noise of the profile.

We computed the profiles for each bin separately and then interpolated the profiles on a finer grid as described in Calisesi et al. (2005) and combined the altitudes of all four bins. We then combined the profiles as a weighted average.

We compute the full width at half maximum of the averaging kernels and divide it by 2.3 to provide the vertical resolution, which is on average 1.4 km and is never higher than 5 km.

3.3. Derivation of Pressure and Temperature Profiles (Step 3)

We use the hydrostatic equilibrium equation to derive a carbon dioxide partial pressure from the previously retrieved carbon dioxide density profile (e.g., Mahieux et al., 2010; Mueller-Wodarg et al., 2008; Snowden et al., 2013).

A difference in pressure Δp_i between two altitudes z_i and z_{i+1} is computed as

$$\Delta p_i = -\int_{z_i}^{z_{i+1}} m\, n(z)\, g(z) dz$$

where m is the carbon dioxide molecular mass and g is the gravitational acceleration computed as

$$g(z) = g_0 \left(\frac{r_M}{r_M + z} \right)^2$$

where r_M is the averaged Mars radius and g_0 is the gravitational acceleration at a tangent altitude $z = 0$. The GMM3 model (Genova et al., 2016) provides g_0 for the corresponding latitude, longitude, and solar longitude corresponding to the occultation and is different from the averaged 3.721 m/s^2 by a maximum of 0.08%. The uncertainties over this value are several orders of magnitude below those of n and are neglected.

To compute the integral in Δp_i, we assume that the natural logarithm of the density varies linearly within the altitudes z_i and z_{i+1}. This is equivalent to assuming a constant scale height h_i between the two altitudes z_i and z_{i+1}

$$h_i = \frac{z_i - z_{i+1}}{\ln\left(\frac{n_{i+1}}{n_i}\right)}.$$

The error induced by this assumption is a function of $\Gamma(z_{i+1} - z_i)/t_i$ where Γ is the lapse rate and t_i is the temperature at z_i. This error depends on the vertical sampling, which is small for NOMAD-SO and the lapse rate is two orders of magnitude lower than the temperature. Therefore, we expect that this error is lower than one percent for NOMAD-SO measurements.

The integration in the expression of Δp_i is usually performed numerically with a trapezoidal rule and we need to consider enough points of integration to retrieve enough accurate solutions (Gröller et al., 2018; Mahieux et al., 2015; Snowden et al., 2013). A form close to an analytical expression is (see Section S6 in Supporting Information S1)

$$\Delta p_i = \frac{m\, g_0\, r_M^2\, n_i}{h_i} \exp(a_i) \left[\frac{E_2(a_i)}{a_i} - \frac{E_2(b_i)}{b_i} \right]$$

where E_2 is an exponential integral

$$E_n(x) = x^{n-1} \int_x^\infty \frac{\exp(-z)}{z^n} dz$$

which is rapidly and accurately computed with an algorithm from the python module scipy.special (Virtanen et al., 2020). We also introduced the reduced altitudes a_i and b_i to simplify the expression with

$$a_i = \frac{r_M + z_i}{h_i}$$

and

$$b_i = \frac{r_M + z_{i+1}}{h_i}.$$

For Mars' atmosphere, both reduced altitudes have values around 300 and 400 between z_i = 0–100 km. The advantage of the analytical form is to avoid the approximation of the minimum number of integration points necessary to compute an accurate solution. The computed value has an accuracy of around 10^{-8}% when using double precision variables.

As we are computing differences in partial pressure between altitudes of the density profile, we need to estimate a partial pressure p_{top} at the uppermost altitude of the profile. We tried several ways to derive p_{top} such as the formula proposed in (Snowden et al., 2013) but the best estimation consists to take the value from GEM-Mars. We take into account uncertainty on this value, which is the upper bound of its variability estimated at 20% (F. Daerden, private communication).

The CO_2 partial pressure profile is computed as

$$p = K_p \Delta p$$

where K_p is an upper triangular matrix of ones and Δp contains the Δp_i with the value for the lowest tangent height at the top and p_{top} at the bottom.

We compute the temperature profile and uncertainties in a similar manner using the ideal gas law. We first compute the differences in temperature

$$\Delta t_i = \frac{\Delta p_i}{k_B n_i}$$

and then the temperature profile

$$t = K_p \, \Delta t.$$

As the formula for Δp_i is a non-linear function of the densities n_i and n_{i+1}, we compute the uncertainties using a Monte Carlo analysis: (a) producing many samples of density profiles considering a normal distribution with n_i as mean and the standard deviation is derived from the uncertainties on n_i, (b) derive the temperature profiles for all samples, and (c) compute the standard deviation on all the temperature profiles. In this case, we need at least 20,000 samples to retrieve the uncertainties with precision lower than 0.0001%. We verified that the first-moment method does not provide enough accurate uncertainties by comparing them to those computed with the Monte Carlo analysis.

The uncertainties are on average 5.0 ± 1.7 K over the entire profile but vary with altitudes and are on average 10.2 ± 3.6 at 2.10^{-2} and 2.1 ± 0.8 K at 4.10^{-1} Pa.

Once the pressure and temperature profiles are retrieved, they can be provided as atmospheric parameters for the slant column retrieval (Section 3.1—Step 1) and another loop is performed until convergence is achieved, i.e. when the last profile is within the error bars of the previously retrieved profile. Convergence usually takes one to three iterations.

4. Results

4.1. Seasonal Variations

Figure 6 shows all the 968 retrieved profiles, 656 in MY 35 and 312 in MY 36. We need to be cautious with the variations in the local time and latitude with orbits. Nevertheless, this set of profiles has several features mainly appearing around 0.1 Pa and at dawn (0 < LST < 12 hr, Figure 6a) as well as at dusk in the Northern hemisphere (12 < LST < 24 hr, Figure 6c). Warm layers appear in all seasons except in the Southern dusk profiles around the aphelion (L_s 50° and 150°). We can also notice stronger warmer layers in the Southern hemisphere around the aphelion (L_s 50°–115°). There is a notable increase in the temperature between L_s 250° and 280° in Northern dawn at pressure levels 0.1–0.01 Pa (see as well Figures 2 and 3 in Part II). Those strong warm layers are treated in more detail in the following paper (Part II).

Some stronger warm layers in the mesosphere at the terminator were reported in some temperature profiles reported in Belyaev et al. (2021—Figure 2b) in MY 35 in the Northern hemisphere and at solar longitudes around 255°–275°, in agreement with the distribution of temperature in Figure 6a. Those warmer layers are also visible in Alday, Trokhimovskiy et al. (2021—Figure 2b) for local times in late morning.

Figure 7 shows the retrieved density at 75 km as a function of solar longitude. As expected (see for instance Forget et al. (2009)), the density is the highest close to perihelion (L_s 251°), the lowest close to aphelion (L_s 71°) and there is roughly a factor of three between them (better seen in Figure 7c). Such a perihelion-aphelion variation can be explained by the variation of the temperature in the lower atmosphere primarily driven by the distance between Mars and the Sun, which controls the scale height of the atmosphere (Forget et al., 2009). The Mars-Sun distance changes by around 20% between aphelion and perihelion, substantially modifying the solar irradiance in a MY. The resulting temperature variation at the poles induces this massive CO_2 condensation inducing a shrinkage of the atmosphere at aphelion and sublimation inducing an expansion of the atmosphere at perihelion (Forget et al., 2009; Hess et al., 1980; Smith, 2008). From Figures 7b and 7d, we see an increase in the density starting from L_s 180° with a peak around L_s 250°. The Southern density is higher than the Northern density closer to Southern summer (solstice at L_s 270°), and we find the inverse around L_s 90°. From Figures 7a and 7c, we might think that the density is a factor of two higher at midnight than at midday for the same solar longitude. But this difference is only apparent as, recalling that SO scans the terminator, midday scans correspond to higher

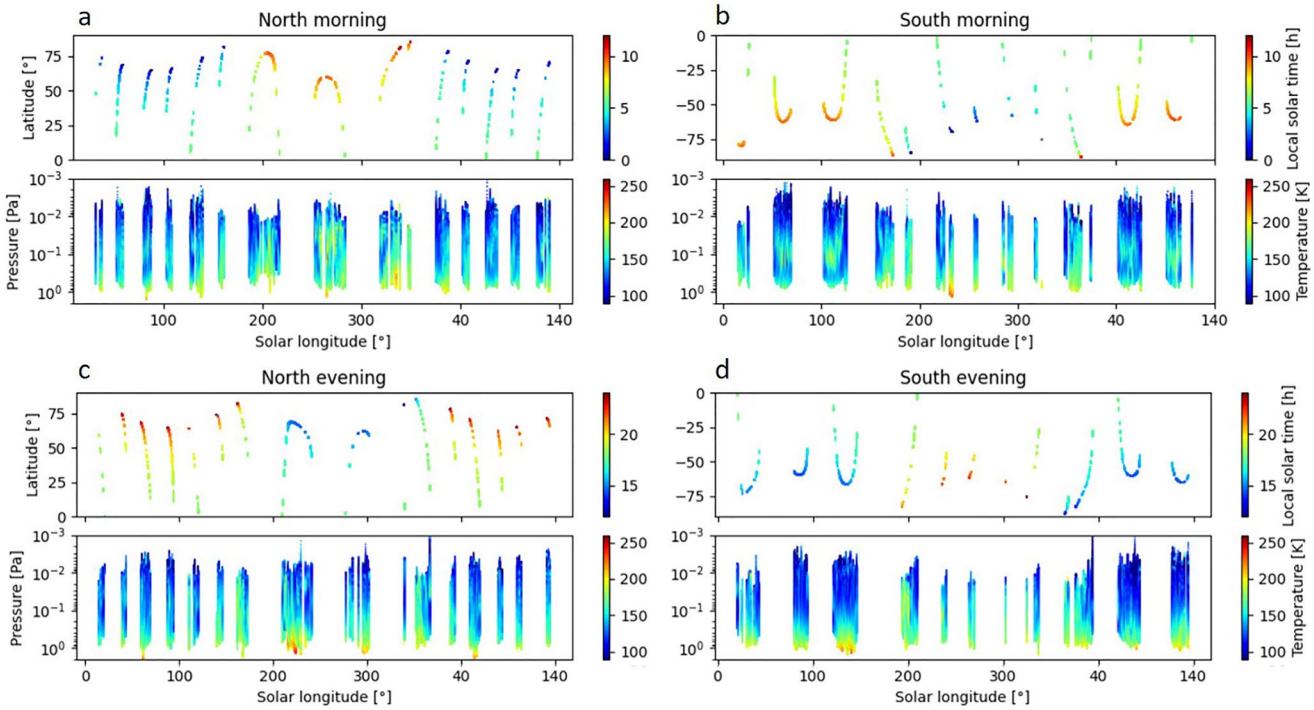

Figure 6. Map of 968 retrieved profiles from Nadir and Occultation for Mars Discovery-Solar Occultation diffraction order 148 for Martian Year (MY) 35 and MY 36 up to L_s 135°. Dawn maps for 0 < LST < 12 hr (a and b) and dusk maps for 12 < LST < 24 hr (c and d). Each vertical bar in the bottom plots represents an independent retrieved profile. Many warmer layers appear (green) in the morning and evening profiles in in the Southern hemisphere evening between 50° and 150° L_s.

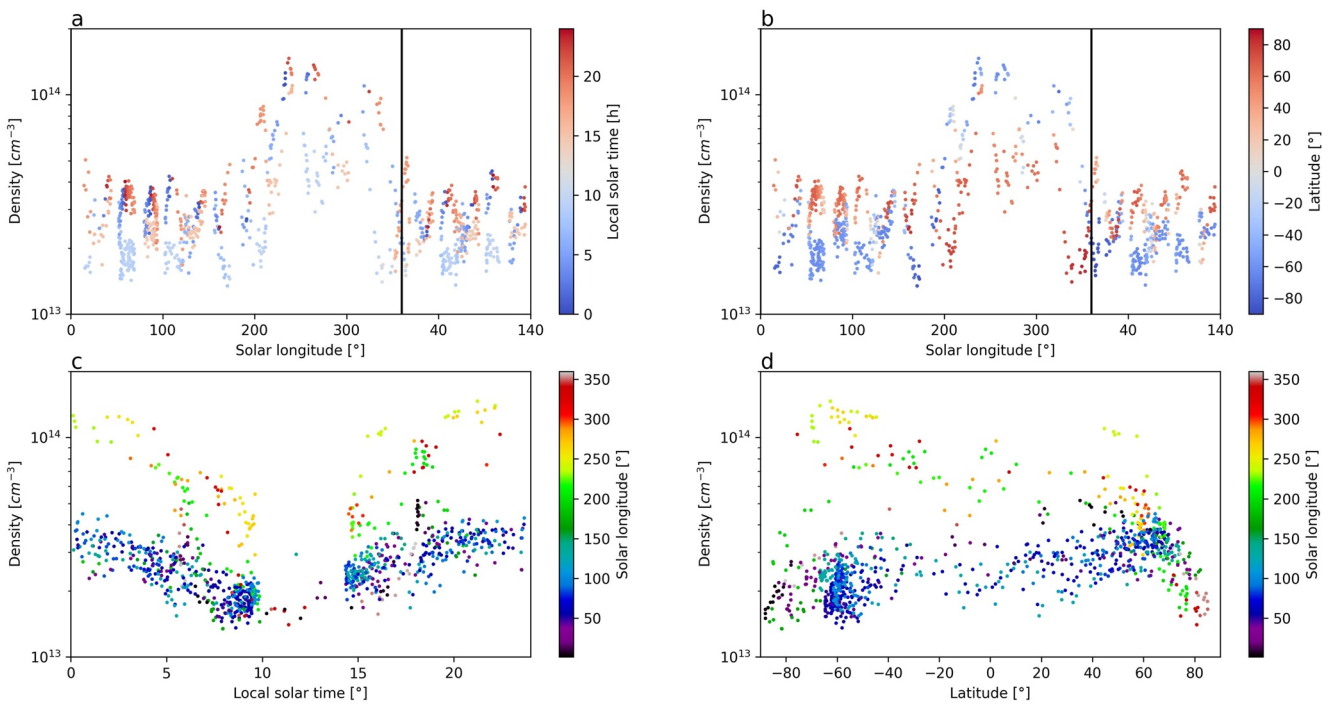

Figure 7. Retrieved CO_2 density at 75 km over Martian Year (MY) 35 and MY 36 until L_s 135° (a and b) as a function of solar longitude, (c) as a function of local solar time, and (d) as a function of latitude. In Panel (a), the color code corresponds to the solar local time, and in panel (b) to the latitude. Local solar time and latitudinal trends are present in panels (a and b).

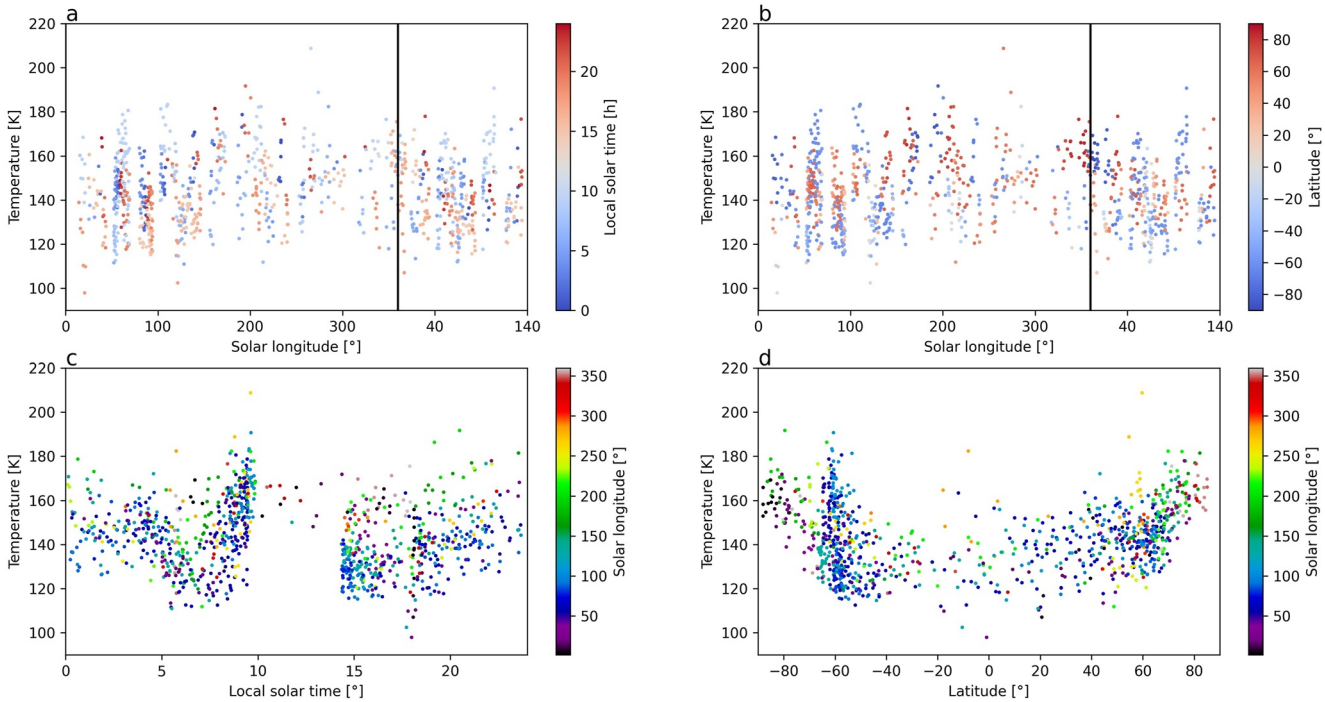

Figure 8. Same as Figure 7 but for temperature as a function of L_s for Martian Year 35 and 36 until L_s 135° and for a pressure of 0.1 Pa.

latitudes in the winter hemisphere while midnight scans correspond to higher latitudes in the hemisphere closer to its summer solstice (see Figure 2).

Figure 8 shows the temperature at 0.1 Pa as a function of solar longitude (Figures 8a and 8b), local solar time (Figure 8c), and latitude (Figure 8d). Figure 8d can be compared for instance with Figure 4 (keeping in mind that this figure represents the nightside) and 5 (dayside) in McCleese et al. (2010) or Figure 8 (zonal mean) in Neary and Daerden (2018) where there is an increase in the temperature toward the poles at 0.1 Pa for all time of the year. This "polar warming" is the result of the adiabatic compression due to the descending branch of the mean meridional circulation (Conrath et al., 2000; McCleese et al., 2008, 2010; McDunn et al., 2013). In the Northern hemisphere, the highest values reach 180 K around 80°N after the Fall equinox and 200 K around 60°N around the winter solstice. As seen in Figures 2a and 2b, the latitudes close to 60°S are more often probed, explaining the larger scatter of values close to 60°S in Figure 8d. Taking this into account, there is a symmetrical distribution of temperature in the Southern hemisphere with higher values around 80°S at equinoxes and higher values around 60°S around Southern winter.

4.2. Latitudinal Variations

Figure 9 shows the latitudinal variations of temperature at dawn between MY 35 (Figures 9e–9h) and MY 36 (Figures 9m–9p). From Figures 9a–9d and Figures 9i–9l, we see that the local time coverage is similar over the 2 years. Comparing Figure 9e and Figure 9m ($L_s < 60°$), there is in both Figure 9a warm layer around 0.1 Pa in the Southern hemisphere that stretches to lower pressures (higher altitudes) with decreasing latitudes. The Northern hemisphere contains structured temperature profiles, especially for the latitudes above 50°. In Figures 9f and 9n ($50° < L_s < 100°$), there are some warmer layers around 0.1 Pa in all the profiles except at the equator, which is not probed in Figure 9f (MY 35). In Figures 9g and 9o ($90 < L_s < 110$), there is still a warm layer around 0.1 Pa in the Southern hemisphere, but it is less clear in the Northern hemisphere where the profiles contain more variations of the temperature gradient along with altitude. In Figures 9h and 9p ($110 < L_s < 140$), there is a warm layer around 0.1 Pa at latitudes around 30°–40°N. In Figure 9h, we see a warmer layer again in the Southern hemisphere that stretches to lower pressures (higher altitudes) as lower latitudes are reached.

Figure 10 shows the latitudinal variation at dusk. Figure 10m ($10° < L_s < 40°$) contains some profiles located at the poles. Those profiles have a higher temperature than the lower latitude ones. From Figures 10g, 10h, 10o,

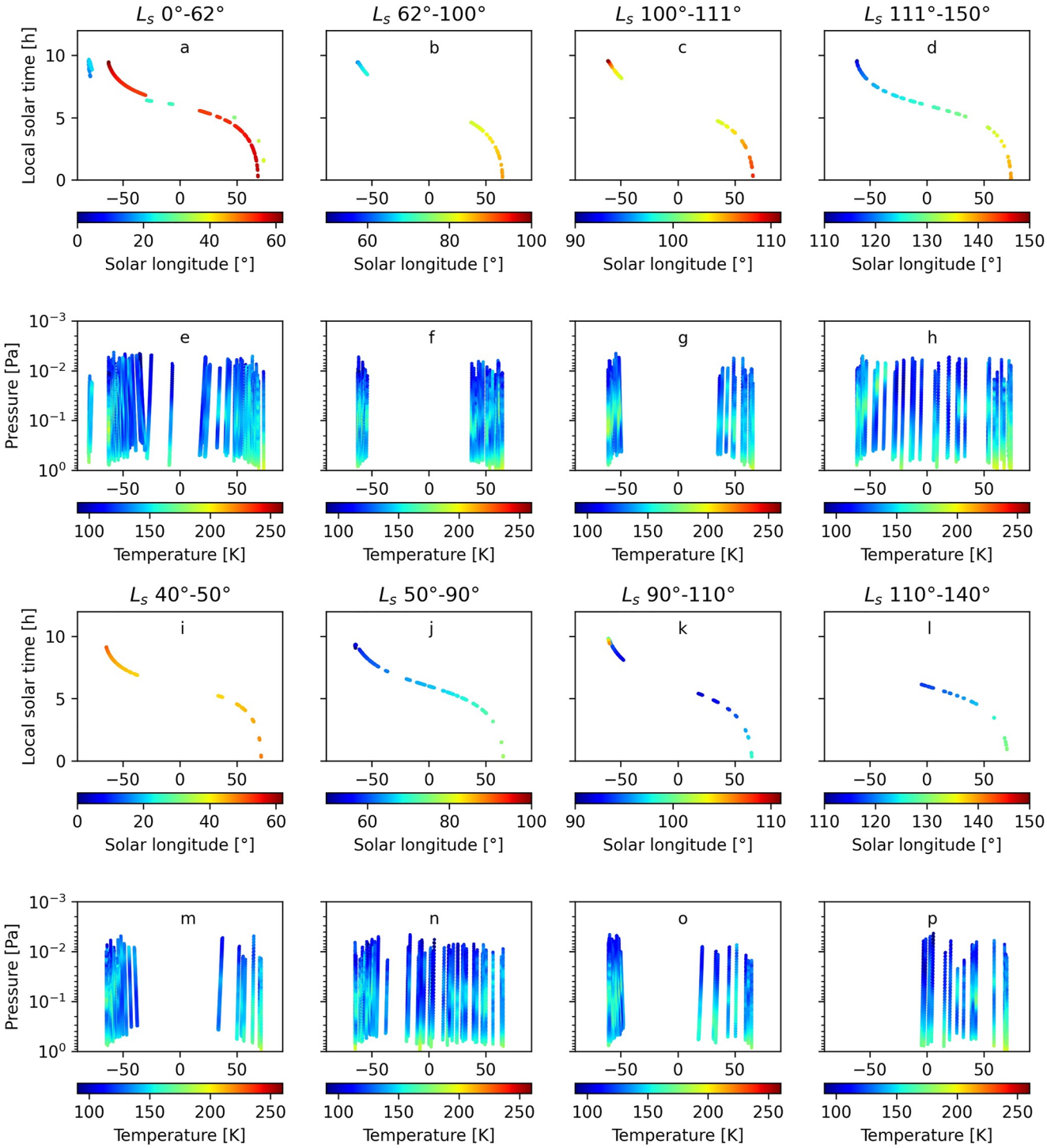

Figure 9. Solar Occultation temperature profiles at dawn (0–12 hr) for (a–h) (a–h) Martian Year (MY) 35 and (i–p) 36 until L_s 140°. Panels (a–d) and (i–l) for solar longitude as a color bar with respect to solar local time (*y*-axis) and latitude (*x*-axis). Panels (e–h) and (m–p) for the temperature profiles as a function of pressure (*y*-axis) and latitude (*x*-axis). The solar longitudes covered in panels (a–d) (MY 35) are roughly similar to those of, respectively, panels (i–l) (MY 36). The local solar times and latitude covered are also roughly similar for the corresponding panels in MY 35 and MY 36.

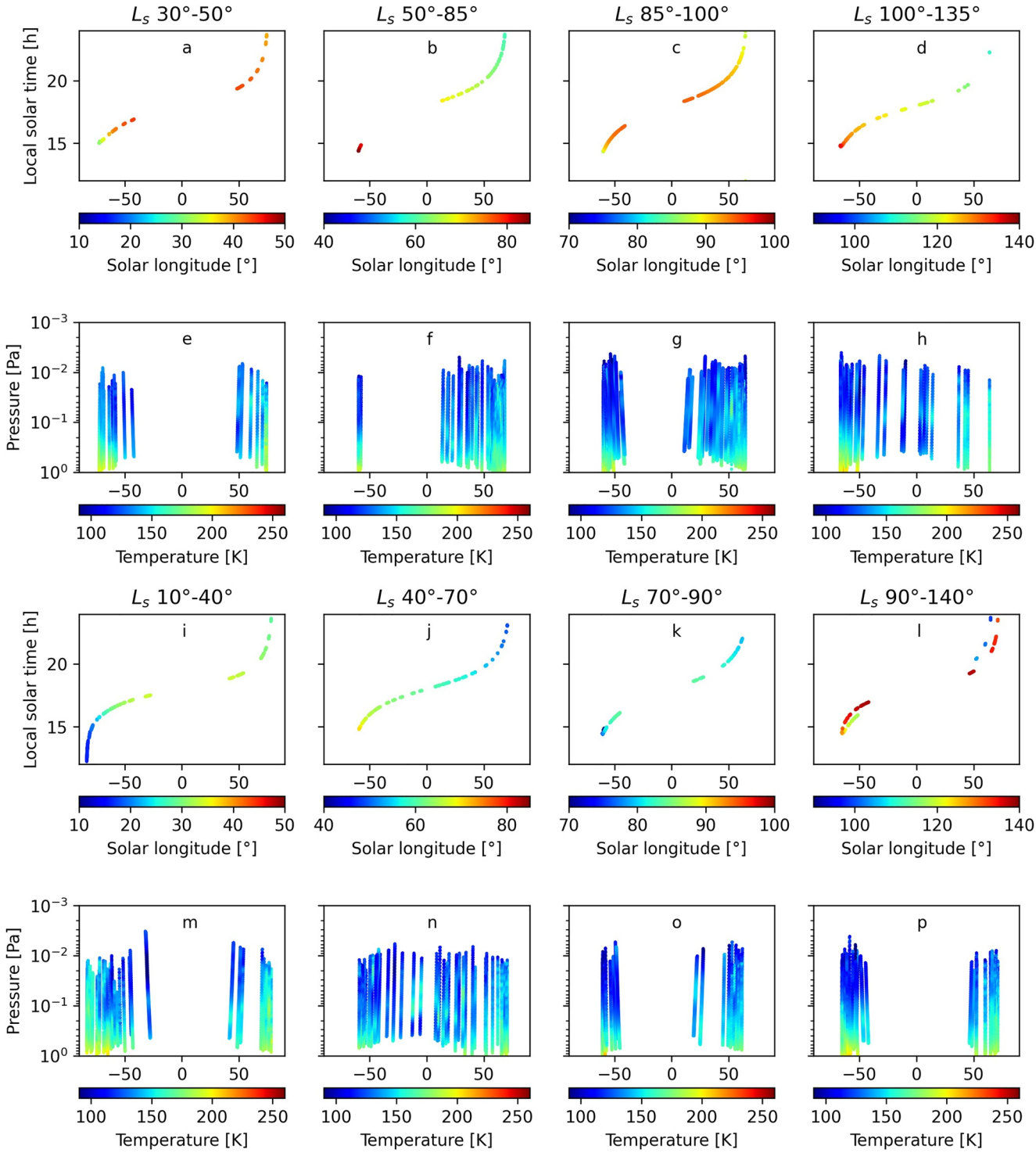

Figure 10. Same as Figure 9 but for dusk (12–24 hr).

and 10p ($70° < L_s < 140°$), we see a cold Southern hemisphere that appears featureless while the Northern hemisphere is hotter and contains several variations in the temperature gradient with altitude. The temperature profiles in Figures 10e, 10m, 10f, and 10n has the same trends with respect to latitude with several variations of the temperature gradient in the Northern hemisphere but a colder Southern hemisphere. An interesting warmer layer around 0.1 Pa appears in several profiles at the equator in Figure 10n (L_s 60°). Those profiles correspond

to evening solar local times and are likely to be related to the warmer feature near the equator reported by Lee et al. (2009) and McCleese et al. (2010) at ~5 to 0.5 Pa and appear to be related to thermal tides.

The results presented above show that the beginnings of MY 35 and MY 36 (L_s 0°–135°) have very similar temperature distributions.

5. Conclusions

This paper presents a retrieval scheme to derive high-resolution vertical profiles of carbon dioxide density, pressure, and temperature from NOMAD-SO measurements of the atmosphere of Mars. Our algorithm aims to derive vertical profiles with excellent information content and fine vertical resolution. The retrieved profiles do not suffer from the presence of any a priori information as in a classical optimal estimation method. The altitude range of the profiles reported in this work extends to where all information on the retrieved profile is taken from the measurement. The excellent information content is achieved by keeping only the retrieved values when the information from the spectra DOF is higher than 0.99 meaning that they are retrieved fully from the spectra. The regularization of the profiles is fine-tuned. We tested seven formulas and we chose to use the expected error estimation method. The saturation of the lines produces a clear bias in the retrieved values at lower altitudes. Those lower altitudes are properly cut using the curve of growth.

To illustrate the retrieved profiles, we focused on a small data set covering the mesosphere region for Martian years 35 and 36 for L_s 0°–135°. The retrieved profiles that cover the Mars terminator show many warmer layers occurring between L_s 50° and 150° in the Northern hemisphere at dawn and dusk but only at dawn in the Southern hemisphere. Comparing the beginning of MY 35 and MY 36 until L_s 135°, these profiles have similar latitudinal and seasonal distributions. Those inversion layers are also described in Part II. The data set presented here serves mainly to show the quality of the data. The full data coverage is three times greater than diffraction order 149 contains twice as many occultations for the time range treated in this preliminary work. The temperature retrieved at the beginning of MY 35 and MY 36 shows the same latitudinal trends.

In Part II of this series of papers, we will present an in-depth analysis of the CO_2 and temperature data set obtained in our study. We will also compare our results with other observations and with GCM simulations.

Data Availability Statement

The results retrieved from the NOMAD measurements used in this article are available on the BIRA-IASB data repository: http://repository.aeronomie.be/?doi=10.18758/71021074 (Trompet & Vandaele, 2022) and are also available from the NOMAD data service through the VESPA portal (http://vespa.obspm.fr). The NOMAD raw data can be found on ESA's planetary science archive (https://archives.esac.esa.int/psa/#!Table%20View/NOMAD=instrument).

Acknowledgments
The NOMAD experiment is led by the Royal Belgian Institute for Space Aeronomy (IASB-BIRA), assisted by Co-PI teams from Spain (IAA-CSIC), Italy (INAF-IAPS), and the United Kingdom (Open University). This project acknowledges funding by the Belgian Science Policy Office (BELSPO), with the financial and contractual coordination by the ESA Prodex Office (PEA 4000103401 and 4000121493), by the Spanish Ministry of Science and Innovation (MCIU), and by European funds under Grants PGC2018-101836-B-I00 and ESP2017-87143-R (MINECO/FEDER), as well as by UK Space Agency through Grants ST/V002295/1, ST/V005332/1, and ST/S00145X/1 and Italian Space Agency through Grant 2018-2-HH.0. This work was supported by the Belgian Fonds de la Recherche Scientifique—FNRS under Grant 30442502 (ET_HOME). This project has received funding from the European Union's Horizon 2020 research and innovation program under Grant 101004052 (RoadMap project). The IAA/CSIC team acknowledges financial support from the State Agency for Research of the Spanish MCIU through the "Center of Excellence Severo Ochoa" award for the Instituto de Astrofísica de Andalucía (SEV-2017-0709) and funding by Grant PGC2018-101836-B-100 (MCIU/AEI/FEDER, EU). G. Villanueva was supported by the National Aeronautics and Space Administration. We thank the two anonymous referees for all their corrections and comments on this manuscript.

References

Alday, J., Trokhimovskiy, A., Irwin, P. G. J., Wilson, C. F., Montmessin, F., Lefévre, F., et al. (2021). Isotopic fractionation of water and its photolytic products in the atmosphere of Mars. *Nature Astronomy*, *5*(9), 943–950. https://doi.org/10.1038/s41550-021-01389-x

Alday, J., Wilson, C. F., Irwin, P. G. J., Trokhimovskiy, A., Montmessin, F., Fedorova, A. A., et al. (2021). Isotopic composition of CO_2 in the atmosphere of Mars: Fractionation by diffusive separation observed by the ExoMars trace gas orbiter. *Journal of Geophysical Research: Planets*, *126*(12), e2021JE006992. https://doi.org/10.1029/2021je006992

Belyaev, D. A., Fedorova, A. A., Trokhimovskiy, A., Alday, J., Montmessin, F., Korablev, O. I., et al. (2021). Revealing a high water abundance in the upper mesosphere of Mars with ACS onboard TGO. *Geophysical Research Letters*, *48*(10), e2021GL093411. https://doi.org/10.1029/2021GL093411

Calisesi, Y., Soebijanta, V. T., & van Oss, R. (2005). Regridding of remote soundings: Formulation and application to ozone profile comparison. *Journal of Geophysical Research*, *110*(23), 1–8. https://doi.org/10.1029/2005JD006122

Conrath, B. J., Pearl, J. C., Smith, M. D., Maguire, W. C., Christensen, P. R., Dason, S., & Kaelberer, M. S. (2000). Mars Global surveyor thermal emission spectrometer (TES) observations: Atmospheric temperatures during aerobraking and science phasing. *Journal of Geophysical Research*, *105*(E4), 9509–9519. https://doi.org/10.1029/1999JE001095

Daerden, F., Neary, L., Villanueva, G., Liuzzi, G., Aoki, S., Clancy, R. T., et al. (2022). Explaining NOMAD D/H observations by cloud-induced fractionation of water vapor on Mars. *Journal of Geophysical Research: Planets*, *127*(2), e2021JE007079. https://doi.org/10.1029/2021JE007079

Daerden, F., Neary, L., Viscardy, S., García Muñoz, A., Clancy, R. T., Smith, M. D., et al. (2019). Mars atmospheric chemistry simulations with the GEM-Mars general circulation model. *Icarus*, *326*, 197–224. https://doi.org/10.1016/j.icarus.2019.02.030

Doicu, A., Trautmann, T., & Schreier, F. (2010). *Numerical regularization for atmospheric inverse problems*. Springer Berlin Heidelberg. https://doi.org/10.1007/978-3-642-05439-6

England, S. L., Liu, G., Kumar, A., Mahaffy, P. R., Elrod, M., Benna, M., et al. (2019). Atmospheric tides at high latitudes in the Martian upper atmosphere observed by MAVEN and MRO. *Journal of Geophysical Research: Space Physics*, *124*(4), 2943–2953. https://doi.org/10.1029/2019JA026601

Fedorova, A. A., Montmessin, F., Korablev, O., Luginin, M., Trokhimovskiy, A., Belyaev, D. A., et al. (2020). Stormy water on Mars: The distribution and saturation of atmospheric water during the dusty season. *Science*, *367*(6475), 297–300. https://doi.org/10.1126/science.aay9522

Forget, F., Montmessin, F., Bertaux, J. L., González-Galindo, F., Lebonnois, S., Quémerais, E., et al. (2009). Density and temperatures of the upper Martian atmosphere measured by stellar occultations with Mars Express SPICAM. *Journal of Geophysical Research*, *114*(1), 1004. https://doi.org/10.1029/2008JE003086

Fornberg, B. (1988). Generation of finite difference formulas on arbitrarily spaced grids. *Mathematics of Computation*, *51*(184), 699–706. https://doi.org/10.2307/2008770

Franz, H. B., Trainer, M. G., Malespin, C. A., Mahaffy, P. R., Atreya, S. K., Becker, R. H., et al. (2017). Initial SAM calibration gas experiments on Mars: Quadrupole mass spectrometer results and implications. *Planetary and Space Science*, *138*, 44–54. https://doi.org/10.1016/j.pss.2017.01.014

Genova, A., Goossens, S., Lemoine, F. G., Mazarico, E., Neumann, G. A., Smith, D. E., & Zuber, M. T. (2016). Seasonal and static gravity field of Mars from MGS, Mars Odyssey and MRO radio science. *Icarus*, *272*, 228–245. https://doi.org/10.1016/j.icarus.2016.02.050

Golub, G. H., Heath, M., & Wahba, G. (1979). Generalized cross-validation as a method for choosing a good ridge parameter. *Technometrics*, *21*(2), 215–223. https://doi.org/10.2307/1268518

Gröller, H., Montmessin, F., Yelle, R. V., Lefèvre, F., Forget, F., Schneider, N. M., et al. (2018). MAVEN/IUVS stellar occultation measurements of Mars atmospheric structure and composition. *Journal of Geophysical Research: Planets*, *123*(6), 1449–1483. https://doi.org/10.1029/2017JE005466

Gröller, H., Yelle, R. V., Koskinen, T. T., Montmessin, F., Lacombe, G., Schneider, N. M., et al. (2015). Probing the Martian atmosphere with MAVEN/IUVS stellar occultations. *Geophysical Research Letters*, *42*(21), 9064–9070. https://doi.org/10.1002/2015GL065294

Hansen, P. C. (1992). Analysis of discrete Ill-posed problems by means of the L-curve. *SIAM Review*, *34*(4), 561–580. https://doi.org/10.1137/1034115

Hess, S. L., Ryan, J. A., Tillman, J. E., Henry, R. M., & Leovy, C. B. (1980). The annual cycle of pressure on Mars measured by Viking Landers 1 and 2. *Geophysical Research Letters*, *7*(3), 197–200. https://doi.org/10.1029/GL007i003p00197

Jain, S. K., Soto, E., Evans, J. S., Deighan, J., Schneider, N. M., & Bougher, S. W. (2021). Thermal structure of Mars' middle and upper atmospheres: Understanding the impacts of dynamics and solar forcing. *Icarus*, *393*, 114703. https://doi.org/10.1016/j.icarus.2021.114703

Koskinen, T. T., Sandel, B. R., Yelle, R. V., Capalbo, F. J., Holsclaw, G. M., McClintock, W. E., & Edgington, S. (2013). The density and temperature structure near the exobase of Saturn from Cassini UVIS solar occultations. *Icarus*, *226*(2), 1318–1330. https://doi.org/10.1016/j.icarus.2013.07.037

Lee, C., Lawson, W. G., Richardson, M. I., Heavens, N. G., Kleinböhl, A., Banfield, D., et al. (2009). Thermal tides in the Martian middle atmosphere as seen by the Mars Climate Sounder. *Journal of Geophysical Research*, *114*(E3), 3005. https://doi.org/10.1029/2008JE003285

Liuzzi, G., Villanueva, G. L., Mumma, M. J., Smith, M. D., Daerden, F., Ristic, B., et al. (2019). Methane on Mars: New insights into the sensitivity of CH_4 with the NOMAD/ExoMars spectrometer through its first in-flight calibration. *Icarus*, *321*, 671–690. https://doi.org/10.1016/j.icarus.2018.09.021

Liuzzi, G., Villanueva, G. L., Trompet, L., Crismani, M. M. J., Piccialli, A., Aoki, S., et al. (2021). First detection and thermal characterization of terminator CO_2 ice clouds with ExoMars/NOMAD. *Geophysical Research Letters*, *48*(22), e2021GL095895. https://doi.org/10.1029/2021gl095895

López-Valverde, M.-A., Funke, B., Brines, A., Stolzenbach, A., Modak, A., Hill, B., et al. (2022). Martian atmospheric temperature and density profiles during the 1st year of NOMAD/TGO solar occultation measurements. *Journal of Geophysical Research: Planets*, e2022JE007278. https://doi.org/10.1029/2022JE007278

Mahieux, A., Vandaele, A. C., Bougher, S. W., Drummond, R., Robert, S., Wilquet, V., et al. (2015). Update of the Venus density and temperature profiles at high altitude measured by SOIR on board Venus Express. *Planetary and Space Science*, *113–114*, 309–320. https://doi.org/10.1016/j.pss.2015.02.002

Mahieux, A., Vandaele, A. C., Neefs, E., Robert, S., Wilquet, V., Drummond, R., et al. (2010). Densities and temperatures in the Venus mesosphere and lower thermosphere retrieved from SOIR on board Venus Express: Retrieval technique. *Journal of Geophysical Research*, *115*(12), E12014. https://doi.org/10.1029/2010JE003589

McCleese, D. J., Heavens, N. G., Schofield, J. T., Abdou, W. A., Bandfield, J. L., Calcutt, S. B., et al. (2010). Structure and dynamics of the Martian lower and middle atmosphere as observed by the Mars Climate Sounder: Seasonal variations in zonal mean temperature, dust, and water ice aerosols. *Journal of Geophysical Research*, *115*(12), 12016. https://doi.org/10.1029/2010JE003677

McCleese, D. J., Schofield, J. T., Taylor, F. W., Abdou, W. A., Aharonson, O., Banfield, D., et al. (2008). Intense polar temperature inversion in the middle atmosphere on Mars. *Nature Geoscience*, *1*(11), 745–749. https://doi.org/10.1038/ngeo332

McCleese, D. J., Schofield, J. T., Taylor, F. W., Calcutt, S. B., Foote, M. C., Kass, D. M., et al. (2007). Mars Climate Sounder: An investigation of thermal and water vapor structure, dust and condensate distributions in the atmosphere, and energy balance of the polar regions. *Journal of Geophysical Research*, *112*(5), 1–16. https://doi.org/10.1029/2006JE002790

McDunn, T., Bougher, S., Murphy, J., Kleinböhl, A., Forget, F., & Smith, M. (2013). Characterization of middle-atmosphere polar warming at Mars. *Journal of Geophysical Research: Planets*, *118*(2), 161–178. https://doi.org/10.1002/jgre.20016

Morozov, V. (1966). On the solution of functional equations by the method of regularization. *Doklady Akademii Nauk SSSR*, *167*(3), 510–512. http://www.mathnet.ru/php/archive.phtml?wshow=paper&jrnid=dan&paperid=32161&option_lang=eng

Mueller-Wodarg, I. C. F., Strobel, D. F., Moses, J. I., Waite, J. H., Crovisier, J., Yelle, R. V., et al. (2008). Neutral atmospheres. *Space Science Reviews*, *139*(1–4), 191–234. https://doi.org/10.1007/s11214-008-9404-6

Nakagawa, H., Jain, S. K., Schneider, N. M., Montmessin, F., Yelle, R. V., Jiang, F., et al. (2020). A warm layer in the nightside mesosphere of Mars. *Geophysical Research Letters*, *47*(4), 1–10. https://doi.org/10.1029/2019GL085646

Nakagawa, H., Terada, N., Jain, S. K., Schneider, N. M., Montmessin, F., Yelle, R. V., et al. (2020). Vertical propagation of wave perturbations in the middle atmosphere on Mars by MAVEN/IUVS. *Journal of Geophysical Research: Planets*, *125*(9), e2020JE006481. https://doi.org/10.1029/2020JE006481

Neary, L., & Daerden, F. (2018). The GEM-Mars general circulation model for Mars: Description and evaluation. *Icarus*, *300*, 458–476. https://doi.org/10.1016/j.icarus.2017.09.028

Neary, L., Daerden, F., Aoki, S., Whiteway, J., Clancy, R. T., Smith, M., et al. (2020). Explanation for the increase in high-altitude water on Mars observed by NOMAD during the 2018 global dust storm. *Geophysical Research Letters*, *47*(7), e2019GL084354. https://doi.org/10.1029/2019GL084354

Neefs, E., Vandaele, A. C., Drummond, R., Thomas, I. R., Berkenbosch, S., Clairquin, R., et al. (2015). NOMAD spectrometer on the ExoMars trace gas orbiter mission: Part 1—Design, manufacturing and testing of the infrared channels. *Applied Optics*, *54*(28), 8494. https://doi.org/10.1364/ao.54.008494

Nelder, J. A., & Mead, R. (1965). A simplex method for function minimization. *The Computer Journa*l, 7(4), 308–313. https://doi.org/10.1093/comjnl/7.4.308

Owen, T., Biemann, K., Rushneck, D. R., Biller, J. E., Howarth, D. W., & Lafleur, A. L. (1977). The composition of the atmosphere at the surface of Mars. *Journal of Geophysical Research*, *82*(28), 4635–4639. https://doi.org/10.1029/js082i028p04635

Phillips, D. L. (1962). A technique for the numerical solution of certain integral equations of the first kind. *Journal of the ACM*, *9*(1), 84–97. https://doi.org/10.1145/321105.321114

Quémerais, E., Bertaux, J. L., Korablev, O., Dimarellis, E., Cot, C., Sandel, B. R., & Fussen, D. (2006). Stellar occultations observed by SPICAM on Mars express. *Journal of Geophysical Research*, *111*(9), 9–13. https://doi.org/10.1029/2005JE002604

Rodgers, C. D. (2000). *Inverse methods for atmospheric sounding* (Vol. 2). World Scientific. https://doi.org/10.1142/3171

Rothman, L. S., & Young, L. D. G. (1981). Infrared energy levels and intensities of carbon dioxide-II. *Journal of Quantitative Spectroscopy and Radiative Transfer*, *25*(6), 505–524. https://doi.org/10.1016/0022-4073(81)90026-1

Sandel, B. R., Gröller, H., Yelle, R. V., Koskinen, T., Lewis, N. K., Bertaux, J. L., et al. (2015). Altitude profiles of O_2 on Mars from SPICAM stellar occultations. *Icarus*, *252*, 154–160. https://doi.org/10.1016/j.icarus.2015.01.004

Saunders, W. R., Person, M. J., & Withers, P. (2021). Observations of gravity waves in the middle atmosphere of Mars. *The Astronomical Journal*, *161*(6), 280. https://doi.org/10.3847/1538-3881/abf1ef

Shirley, J. H., McConnochie, T. H., Kass, D. M., Kleinböhl, A., Schofield, J. T., Heavens, N. G., et al. (2015). Temperatures and aerosol opacities of the Mars atmosphere at aphelion: Validation and inter-comparison of limb sounding profiles from MRO/MCS and MGS/TES. *Icarus*, *251*, 26–49. https://doi.org/10.1016/j.icarus.2014.05.011

Smith, M. D. (2008). Spacecraft observations of the Martian atmosphere. *Annual Review of Earth and Planetary Sciences*, *36*(1), 191–219. https://doi.org/10.1146/annurev.earth.36.031207.124334

Snowden, D., Yelle, R. V., Cui, J., Wahlund, J.-E. E., Edberg, N. J. T. T., & Ågren, K. (2013). The thermal structure of Titan's upper atmosphere, I: Temperature profiles from Cassini INMS observations. *Icarus*, *226*(1), 552–582. https://doi.org/10.1029/2010JA016251

Starichenko, E. D., Belyaev, D. A., Medvedev, A. S., Fedorova, A. A., Korablev, O. I., Trokhimovskiy, A., et al. (2021). Gravity wave activity in the Martian atmosphere at altitudes 20–160 km from ACS/TGO occultation measurements. *Journal of Geophysical Research: Planets*, *126*(8), e2021JE006899. https://doi.org/10.1029/2021JE006899

Steck, T. (2002). Methods for determining regularization for atmospheric retrieval problems. *Applied Optics*, *41*(9), 1788. https://doi.org/10.1364/ao.41.001788

Thomas, I. R., Aoki, S., Trompet, L., Robert, S., Depiesse, C., Willame, Y., et al. (2021). Calibration of NOMAD on ESA's ExoMars trace gas orbiter: Part 1 – The solar occultation channel. *Planetary and Space Science*, *218*, 105411. https://doi.org/10.1016/j.pss.2021.105411

Tikhonov, A. N. (1963). Solution of incorrectly formulated problems and the regularization method. *Soviet Mathematics - Doklady*, *4*, 1035–1038.

Trompet, L., Mahieux, A., Ristic, B., Robert, S., Wilquet, V., Thomas, I. R., et al. (2016). Improved algorithm for the transmittance estimation of spectra obtained with SOIR/Venus express. *Applied Optics*, *55*(32), 9275. https://doi.org/10.1364/ao.55.009275

Trompet, L., & Vandaele, A. C. (2022). Subset of CO_2 and temperature vertical profiles retrieved from NOMAD-SO/TGO, presented in Trompet et al. 2022 [Dataset]. Royal Belgian Institute for Space Aeronomy. https://doi.org/10.18758/71021074

Trompet, L., Vandaele, A. C., Thomas, I., Aoki, S., Daerden, F., Erwin, J., et al. (2023). Carbon dioxide retrievals from NOMAD-SO on ESA's ExoMars Trace Gas Orbiter and temperature profile retrievals with the hydrostatic equilibrium equation: 2. Temperature variabilities in the mesosphere at Mars terminator. *Journal of Geophysical Research: Planets*, *128*, e2022JE007279. https://doi.org/10.1029/2022JE007279

Twomey, S. (1963). On the numerical solution of Fredholm integral equations of the first kind by the inversion of the linear system produced by quadrature. *Journal of the ACM*, *10*(1), 97–101. https://doi.org/10.1145/321150.321157

Vandaele, A. C., Kruglanski, M., & De Mazière, M. (2006). *Modeling and retrieval of atmospheric spectra using ASIMUT* (p. 618). European Space Agency, (Special Publication) ESA SP.

Vandaele, A. C., Neefs, E., Drummond, R., Thomas, I. R. R., Daerden, F., Lopez-Moreno, J.-J. J., et al. (2015). Science objectives and performances of NOMAD, a spectrometer suite for the ExoMars TGO mission. *Planetary and Space Science*, *119*, 233–249. https://doi.org/10.1016/j.pss.2015.10.003

Villanueva, G. L., Liuzzi, G., Aoki, S., Stone, S. W., Brines, A., Thomas, I. R., et al. (2022). The deuterium isotopic ratio of water released from the Martian caps as measured with TGO/NOMAD. *Geophysical Research Letters*, *49*(12), e2022GL098161. https://doi.org/10.1029/2022GL098161

Virtanen, P., Gommers, R., Oliphant, T. E., Haberland, M., Reddy, T., Cournapeau, D., et al. (2020). SciPy 1.0: Fundamental algorithms for scientific computing in Python. *Nature Methods*, *17*(3), 261–272. https://doi.org/10.1038/s41592-019-0686-2

Xu, J., Schreier, F., Doicu, A., & Trautmann, T. (2016). Assessment of Tikhonov-type regularization methods for solving atmospheric inverse problems. *Journal of Quantitative Spectroscopy and Radiative Transfer*, *184*, 274–286. https://doi.org/10.1016/j.jqsrt.2016.08.003